Temporally controlled multistep division of DNA droplets for dynamic artificial cells

Tomoya Maruyama[1], Jing Gong[1], Masahiro Takinoue[1,2,3,*]

[1] Department of Life Science and Technology, Tokyo Institute of Technology, 4259 Nagatsuta-cho, Midori-ku, Yokohama, Kanagawa 226-8501, Japan
[2] Department of Computer Science, Tokyo Institute of Technology, 4259 Nagatsuta-cho, Midori-ku, Yokohama, Kanagawa 226-8501, Japan
[3] Living Systems Materialogy (LiSM) Research Group, International Research Frontiers Initiative (IRFI), Tokyo Institute of Technology, 4259 Nagatsuta-cho, Midori-ku, Yokohama, Kanagawa 226-8501, Japan

*E-mail: takinoue@c.titech.ac.jp

1

Abstract

Bio-soft matter droplets formed via liquid-liquid phase separation (LLPS) of biopolymers have been found in living cells. Synthetic LLPS droplets have recently been employed in nanobiotechnology for artificial cell construction, molecular robotics, molecular computing, diagnosis, and therapeutics. Controlling the dynamics of bio-soft matter droplets is essential for developing such bio-inspired functional systems because living systems maintain their functions based on the temporally controlled dynamics of biomolecular reactions and assemblies. Recently, the dynamics of bio-soft matter droplets have been revealed; however, their temporal control has not yet been achieved. This paper reports the temporal control of DNA-based LLPS droplets (DNA droplets). We demonstrate the timing-controlled division of DNA droplet-based artificial cells via time-delayed division triggers regulated by non-equilibrium chemical reactions. We also investigated it using a reaction-diffusion model. We regulated the release order of multiple division triggers, resulting in order control of the multistep droplet division, that is, pathway control of the droplet division in a reaction landscape. Finally, we demonstrate an application of the timing-controlled division of DNA droplet-based artificial cells: a molecular computing element to compare the concentrations of microRNA sequences (called molecular comparators). We believe that temporal control of DNA droplets will promote the design of more dynamic artificial cells/molecular robots and more sophisticated biomedical applications.

Introduction

Living cells exhibit well-organized dynamics in bio-soft matter assemblies, such as membrane deformation, cell division, and cell differentiation[1], which are essential features that distinguish living systems from non-living matter. Recently, liquid-liquid phase separation (LLPS) droplets of bio-soft matter have been found in living cells, and their dynamic behaviors have attracted attention[2,3], such as nucleolar assembly through non-equilibrium processes of rRNA transcription[4], sol-gel transition[5], and activation/inhibition of molecular reactions[6]. These examples show that precise temporal control of biological LLPS droplets via non-equilibrium chemical reactions realizes such dynamic behaviors.

Synthetic LLPS droplets have recently been explored in bottom-up synthetic biology for constructing artificial cells[7,8], molecular robots[9], molecular computers[10,11], and biomedical nanodevices[12]. Various dynamic behaviors of synthetic LLPS droplets have been reported, such as sequestration of molecules[13–15], motion[9,16], and division[17]. More recently, non-equilibrium dynamics such as cyclic assembly/disassembly[18,19] and transient shell-formation[20] of synthetic coacervate droplets were achieved by coupling LLPS droplets with non-equilibrium chemical reactions such as phosphorylation/dephosphorylation[21,22] and enzymatic synthesis of polynucleotide[23]. However, temporal control of LLPS droplet dynamics remains difficult. Programmable temporal control methods must be developed to mimic cell dynamics.

DNA is well known for its programmable structures[24,25] and reactions[26]. DNA programmability also facilitates the temporal control of chemical reactions. For example, DNA computing reactions have been demonstrated, such as the chemical oscillation of DNA concentrations[27–29], temporal logic circuit[30], and timing-controlled generation of chemical signals[31,32]. Moreover, the programmability of DNA has been utilized not only for controlling chemical reactions but also for controlling the physical dynamics of mechanical DNA-based nanostructures[33–35]. Particularly, DNA-based coacervates[36,37] (also referred to as DNA droplets) formed with branched DNA nanostructures[17,38–45] can couple physical dynamics with chemical reactions in a programmable manner. DNA droplets divide autonomously with enzymatic[17] and photo[41] cleavage reactions and locomotion via enzymatic degradation[16,46]. Phase separation of DNA droplets based on molecular logic computation[47] and reaction-diffusion pattern formation coupled with RNA transcription and diffusion[48] have also been demonstrated. However, achieving the

3

timing-controlled physical dynamics of DNA droplets coupled with non-equilibrium chemical reactions remains challenging.

In the present study, we demonstrated the timing-controlled division dynamics of DNA droplet-based artificial cells by coupling them with non-equilibrium chemical reactions, resulting in the pathway control of artificial cell division (Figure 1). We used DNA droplets constructed by mixing two Y-shaped branched DNA nanostructures (Y_A and Y_B; called binary-mixed DNA droplets), in which 6-branched DNA linkers crosslinked Y_A and Y_B (Figures 2a and 2b). Mixed DNA droplets are divided into Y_A and Y_B by cleaving the DNA linkers through the hybridization with division trigger DNAs. Here, we coupled the mixed DNA droplet with non-equilibrium chemical reactions; the time delay of division triggers (Figure 1a) realized timing and pathway control of DNA droplet division (Figures 1b-1d). We used temporal control of DNA reactions based on RNA degradation with a ribonuclease H (RNase H), which has been used in many dynamic DNA reactions such as DNA oscillators[27], DNA bistable switch[49], logic computation[50], DNA walker[51], and timers for DNA strand displacement reactions[31,32]; however, there is no report on temporal control of LLPS droplets with the RNase H reaction. Finally, we present a molecular computing element to compare the concentrations of microRNA (miRNA) sequences (called molecular comparators) as an application of the timing-controlled division of DNA-droplet-based artificial cells. Our results provide a method for chemically regulating the timing-controlled physical dynamics of LLPS droplets for artificial cell studies.
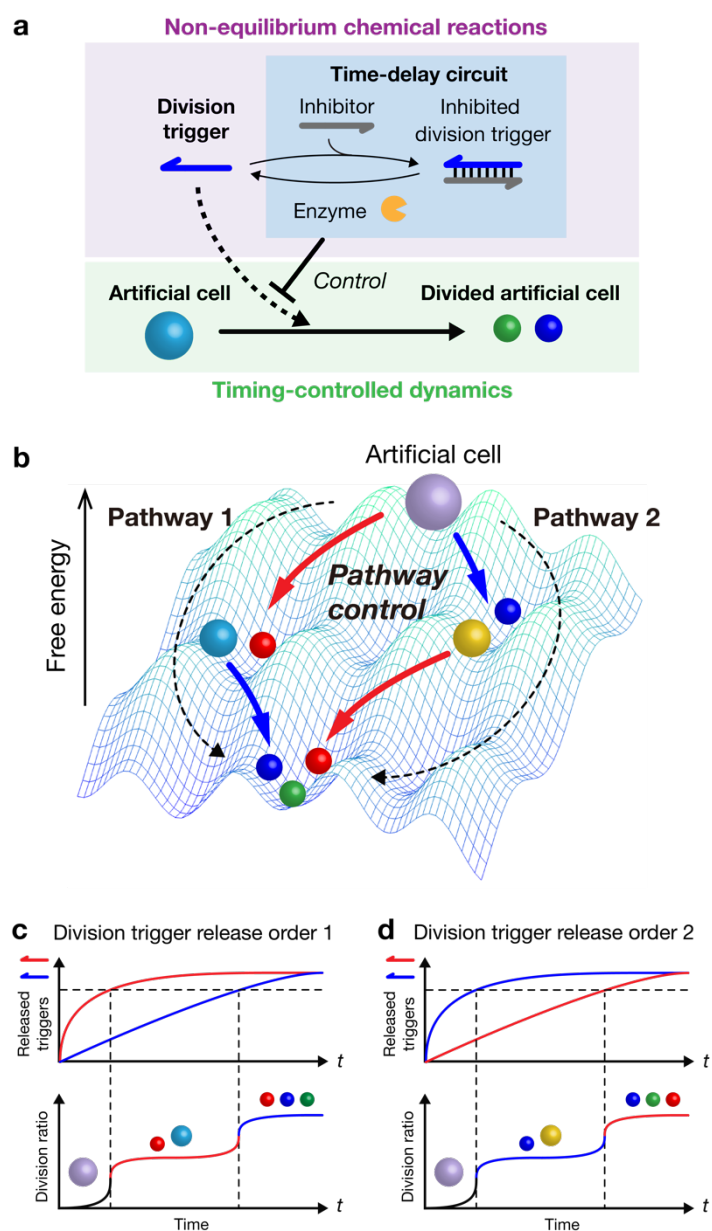
4

Figure 1. Conceptual illustration of timing control of artificial cell division via non-equilibrium chemical reactions. (**a**) Timing-controlled division of an artificial cell regulated by a time-delay circuit. (**b**) Pathway-controlled division of DNA droplet-based artificial cells. (**c** and **d**) Time-delay circuits control division pathways by changing the release order of different division triggers.

Results and discussion

Autonomous division of binary-mixed DNA droplets using division trigger DNAs

Figure 2a shows the design of DNA droplets for artificial cells. Y-shaped branched DNA nanostructures self-assemble to form DNA droplets via hybridization of self-complementary sticky ends at their branches[17]. Because Y_A and Y_B have non-complementary sticky ends (Figure 2b; detailed sequences are in Supplemental Table S1), the resultant A- and B-droplets do not fuse; however, a 6-branched DNA linker (L_{AB}) (Figure 2b; Supplemental Table S2) can crosslink Y_A and Y_B, forming a binary-mixed DNA droplet (A·B-droplet) (Figure 2b). Here, '·' (a single center dot) in 'A·B' indicates that one type of linker (L_{AB}) crosslinks Y_A and Y_B in A·B-droplet. Figure 2c shows confocal laser scanning microscopy (CLSM) images of the A·B-droplet. The A·B-droplet can be divided by cleaving L_{AB} into two portions (Figure 2d). For L_{AB} cleavage, we used a nucleic acid strand displacement reaction induced by single-stranded DNA (ssDNA) division triggers (T_{AB1} and T_{AB2})[47] (Figure 2e). The division triggers hybridize to the toehold sequences ($Toehold_{AB1}$ and $Toehold_{AB2}$) in L_{AB} and invade the branches of L_{AB} via strand-displacement reactions (Figure 2e, middle), cleaving L_{AB} into two portions (Figure 2e, right). Considering the reaction landscape (Figure 2f), the L_{AB} cleavage reaction uses division triggers as chemical "fuels"[29]. After adding the division triggers, the cleaved-L_{AB} is more stable than the initial L_{AB} because of the Gibbs free energy change (ΔG_{Clv}) induced by division trigger hybridization and strand displacement reactions. Thus, cleavage is a non-equilibrium chemical reaction that uses chemical energy. Figure 2g shows the time-lapse images of the division of the A·B-droplet after adding the division triggers. The A·B-droplet started to divide just after adding division triggers.
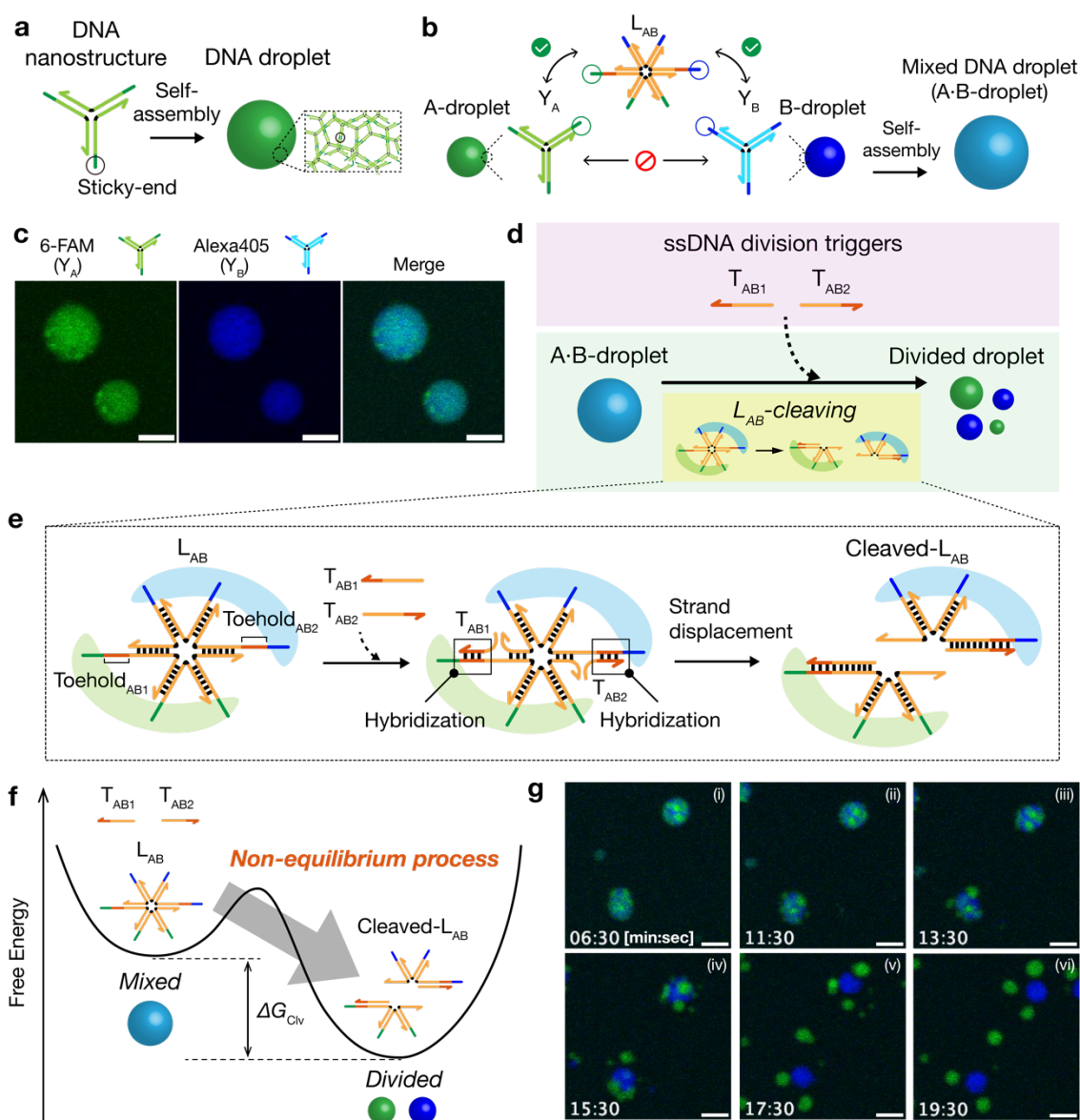
6

Figure 2. Design of binary-mixed DNA droplets. (**a**) Schematic of DNA droplet formation. Y-shaped branched DNA nanostructures self-assemble via binding of palindromic sticky ends, forming a DNA droplet. (**b**) Binary-mixed DNA droplet formation. Sticky ends of Y_A and Y_B are crosslinked by 6-branched DNA linker L_{AB}. After the self-assembly of these DNA nanostructures, a binary-mixed DNA droplet (A·B-droplet) is formed. (**c**) CLSM images of A·B-droplets. Green: Y_A labeled with 6-carboxyfluorescein (6-FAM); Blue: Y_B labeled with Alexa Fluor® 405 (Alexa405). Co-localization of Y_A and Y_B was observed. Scale bars: 10 μm. (**d** and **e**) Division of A·B-droplet via L_{AB} cleavage. L_{AB} is designed to be cleaved by a strand-displacement reaction with ssDNA division triggers (T_{AB1} and T_{AB2}). (**f**) Reaction landscape describing the division of A·B-droplet. The ssDNA division triggers work as "fuel" molecules to drive

a strand displacement reaction to cleave L_{AB}. (**g**) Time-lapse images of division of A·B-droplets. Scale bars: 10 μm.

Design of timing-control of DNA droplet division based on time-delay circuits

We hypothesized that inhibiting "active" division triggers causes the time delay of the linker cleavage, resulting in timing control over DNA droplet division. Figure 3a shows the design of a time-delay circuit comprising reactions (i) and (ii). (i) Active division triggers changed to inhibited division triggers by the hybridization of excess single-stranded RNAs (ssRNAs), named inhibitor RNAs. (ii) An RNase H degrades the inhibitor RNAs in the inhibited division triggers, thereby releasing active division triggers. These two reactions cause a time delay in the cleavage of the DNA linker.

To tune the time delay of the binary-mixed DNA droplet division, we introduced $L^{\dagger}_{AB}$ in addition to the original DNA linker, L_{AB} (Figure 3b). We describe this binary-mixed DNA droplet as "A:B-droplet," where ':' (double dots) indicates that Y_A and Y_B are crosslinked with two DNA linkers, L_{AB} and $L^{\dagger}_{AB}$. A:B-droplets divide only when both L_{AB} and $L^{\dagger}_{AB}$ are cleaved. In addition, linkers and triggers with "†" indicate those that can achieve a time delay in the presence of inhibitor RNAs and RNase H (Figure 3c). L_{AB} is cleaved by the active division triggers T_{ABi} (i=1, 2), while $L^{\dagger}_{AB}$ is cleaved by active division triggers $T^{\dagger}_{ABi}$ (i=1, 2). Inhibitor RNAs $R^{\dagger}_{ABi}$ hybridize with $T^{\dagger}_{ABi}$, and form inhibited division triggers $iT^{\dagger}_{ABi}$, inducing the time delay of A:B-droplet division. This time-delay circuit was inspired by intracellular time-delay control via reaction suppression based on small RNA expression[52]. For such biological meaning and applications shown later, we used natural miRNA sequences, miR-6875-5p and miR-4634[47,53], for $R^{\dagger}_{ABi}$ sequences, respectively (Supplemental Table S3); that is, if either of the miRNAs exist, the A:B-droplet division is delayed.

Numerical investigations of timing-control of DNA droplet division

First, we numerically investigated the dependence of the cleaving rate of $L^{\dagger}_{AB}$ on the concentrations of RNase H and the inhibitor RNAs ($R^{\dagger}_{ABi}$; i=1, 2) using a reaction-diffusion model. The following are some of the partial differential equations (see Supplemental Note S1 for details):

8

$$\frac{\partial u_{\mathrm{T}^\dagger_{\mathrm{AB}i}}}{\partial t} = D(\boldsymbol{x})\nabla^2 u_{\mathrm{T}^\dagger_{\mathrm{AB}i}} + f\left(u_{\mathrm{T}^\dagger_{\mathrm{AB}i}}, u_{\mathrm{L}^\dagger_{\mathrm{AB}}}, \cdots\right) + g\left(u_{\mathrm{T}^\dagger_{\mathrm{AB}i}}, u_{\mathrm{R}^\dagger_{\mathrm{AB}i}}, u_{\mathrm{iT}^\dagger_{\mathrm{AB}i}}\right), \qquad (1)$$

$$\frac{\partial u_{\mathrm{L}^\dagger_{\mathrm{AB}}}}{\partial t} = D(\boldsymbol{x})\nabla^2 u_{\mathrm{L}^\dagger_{\mathrm{AB}}} - \sum_{i=1,2} k_{\mathrm{h}_{\mathrm{AB}}} u_{\mathrm{L}_{\mathrm{AB}}} u_{\mathrm{T}^\dagger_{\mathrm{AB}i}}, \qquad (2)$$

$$g\left(u_{\mathrm{T}^\dagger_{\mathrm{AB}i}}, u_{\mathrm{R}^\dagger_{\mathrm{AB}i}}, u_{\mathrm{iT}^\dagger_{\mathrm{AB}i}}\right) \equiv \frac{k_{\mathrm{cat}} c_{\mathrm{E}_{\mathrm{RH}}} u_{\mathrm{iT}^\dagger_{\mathrm{AB}i}}}{K_{\mathrm{m}} + u_{\mathrm{iT}^\dagger_{\mathrm{AB}i}}} - k_{\mathrm{h}_{\mathrm{RNA}}} u_{\mathrm{T}^\dagger_{\mathrm{AB}i}} u_{\mathrm{R}^\dagger_{\mathrm{AB}i}}. \qquad (3)$$

The partial differential equations express the spatiotemporal change of the division triggers $\mathrm{T}^\dagger_{\mathrm{AB}i}$ (i = 1, 2) and the linker $\mathrm{L}^\dagger_{\mathrm{AB}}$; u_{X} is the concentration of molecule "X." The first terms in Eqs. 1 and 2 denote the spatial diffusion of $\mathrm{T}^\dagger_{\mathrm{AB}i}$ and $\mathrm{L}^\dagger_{\mathrm{AB}}$, respectively; $D(\boldsymbol{x})$ is the diffusion coefficient depending on the position $\boldsymbol{x}$ ($\boldsymbol{x}$ = "inside" or "outside" of A:B-droplet). The term $f(\cdots)$ denotes the consumption of division triggers $\mathrm{T}^\dagger_{\mathrm{AB}1}$ via hybridization with $\mathrm{L}^\dagger_{\mathrm{AB}}$ and other molecules (details in Supplemental Note S1). $g(\cdots)$ denotes the time delay reaction (defined by Eq.3), modulated by the concentrations of RNase H and the inhibitor RNAs; K_{m} and k_{cat} are the Michaelis-Menten parameters for the RNase H reaction; $c_{\mathrm{E}_{\mathrm{RH}}}$ is the total RNase H concentration; $k_{\mathrm{h}_{\mathrm{AB}}}$ and $k_{\mathrm{h}_{\mathrm{RNA}}}$ are the hybridization rates of the division triggers with linker L_{AB} and the inhibitor RNAs, respectively. The second term of Eq.2 denotes the hybridizations of $\mathrm{L}^\dagger_{\mathrm{AB}}$ with $\mathrm{T}^\dagger_{\mathrm{AB}i}$. We also obtained partial differential equations for the other molecules; the details of the full numerical model and numerical simulations are described in Supplemental Note S1.

Figures 3d and 3e show the distributions of L_{AB} and $\mathrm{L}^\dagger_{\mathrm{AB}}$, respectively, in an A:B-droplet at several normalized simulation time steps (the white broken-line circle indicates the surface of the A:B-droplet). In the present study, we fixed the percentages of L_{AB} and $\mathrm{L}^\dagger_{\mathrm{AB}}$ to the total amount of linker DNA to 90% and 10%, respectively. We referred to previously reported kinetic parameters and diffusion coefficients[50,54–57]. The results show that $\mathrm{L}^\dagger_{\mathrm{AB}}$ remains longer than L_{AB}, although the percentage of $\mathrm{L}^\dagger_{\mathrm{AB}}$ is lower than that of L_{AB}. This indicates that the decrease of $\mathrm{L}^\dagger_{\mathrm{AB}}$ becomes slower due to the time-delay circuit.

We investigated the dependence of the decreasing rate of total DNA linkers (L_{AB} and $\mathrm{L}^\dagger_{\mathrm{AB}}$) on the $c_{\mathrm{E}_{\mathrm{RH}}}$ and the initial concentration of the inhibitor RNAs ($u^0_{\mathrm{R}^\dagger_{\mathrm{AB}i}}$; i = 1, 2) (Figure 3f and 3g). The decreasing rate of the total DNA linkers becomes slower by decreasing $c_{\mathrm{E}_{\mathrm{RH}}}$ or increasing $u^0_{\mathrm{R}^\dagger_{\mathrm{AB}i}}$. This is because the decreasing rate of $\mathrm{L}^\dagger_{\mathrm{AB}}$ gets slower upon decreasing $c_{\mathrm{E}_{\mathrm{RH}}}$ or increasing $u^0_{\mathrm{R}^\dagger_{\mathrm{AB}i}}$ (Supplemental Figure S1). Here, we

assumed that the division ratio of the A:B-droplets followed a sigmoidal cooperative function of the total concentration of uncleaved linkers w (Supplemental Note S1):

$$H(w) = \frac{K^n}{K^n + w^n} \, , \tag{4}$$

$$r_{\text{div}} = \frac{H(w) - H_{\min}}{H_{\max} - H_{\min}} \, , \tag{5}$$

where K is the threshold concentration of the uncleaved linker for A:B-droplet division and n is a cooperativity coefficient that expresses the switch-like dependence of division on w. $H_{\max}$ and $H_{\min}$ are the maximum and minimum values of $H(w)$, respectively. The cooperative switch-like dependence expressed by the Hill-type function $H(w)$ was observed by Gong et al.[47]; cooperative nonlinear behavior is observed because the cleavage of most linkers is necessary for DNA droplet division. Figures 3h and 3i show the time courses of r_{div} when changing $c_{E_{RH}}$, and $u^0_{R^\dagger_{ABi}}$ with $K = 0.95$ and $n = 16$ fixed. Consequently, the r_{div} increases at a slower rate by decreasing $c_{E_{RH}}$ or increasing $u^0_{R^\dagger_{ABi}}$. This trend did not change depending on values of K and n (Supplemental Figure S2). Therefore, these results suggest that the timing of the division can be controlled by tuning the decreasing rate of $L^\dagger_{AB}$.
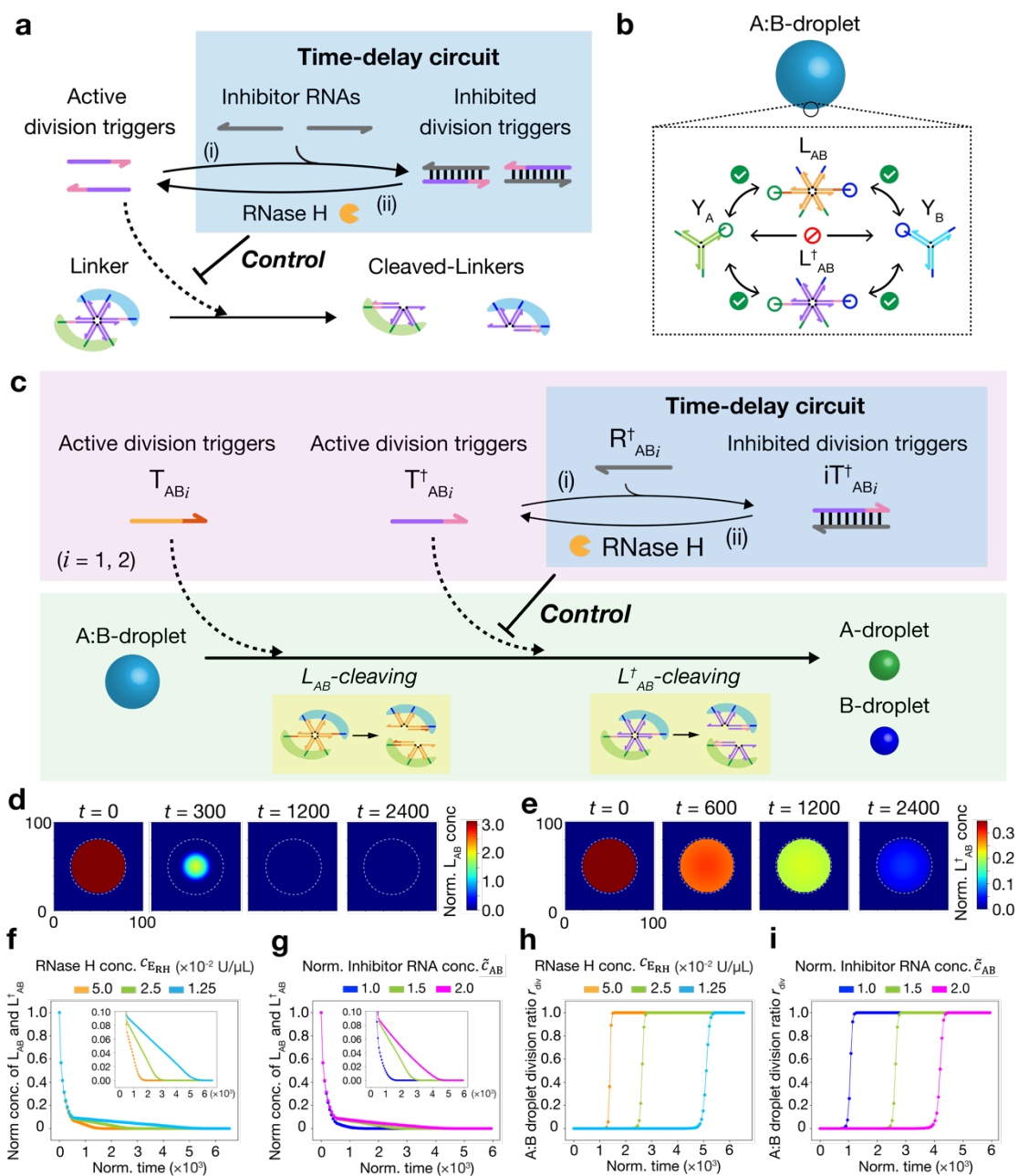
10

Figure 3. Numerical investigation of timing-controlled linker-cleavage for DNA droplet division. (**a**) Schematics of time-delay circuit to regulate cleaving rate of a DNA linker. (i) Excess inhibitor RNAs hybridize with active division triggers, producing inhibited division triggers. (ii) Active division triggers are released from inhibited division triggers by RNase H reaction. Note that inhibitor RNAs not forming inhibited division triggers are not degraded by RNase H because RNase H degrades only RNAs

11

forming duplexes with DNAs. Released active division triggers hybridize with the DNA linker, cleaving the linker via strand displacement. **(b)** Compositions of a binary-mixed DNA droplet (A:B-droplet). (**c**) Schematic of the timing-controlled division of A:B-droplet using a time-delay circuit. L_{AB} is initially cleaved using T_{ABi} followed by the cleaving of $L^{\dagger}_{AB}$, resulting in the division of A:B-droplet. The time-delayed cleaving of $L^{\dagger}_{AB}$ is achieved by the release of $T^{\dagger}_{ABi}$ from $iT^{\dagger}_{ABi}$. The degree of time delay of the $T^{\dagger}_{ABi}$ release decides the timing control of the droplet division. $R^{\dagger}_{ABi}$ ($i = 1, 2$) sequences are miR-6875-5p and miR-4634, respectively. Linkers and triggers with "†" indicate those that can achieve a time-delay circuit if inhibitor RNAs and RNase H are added. (**d** and **e**) Snapshots of numerically calculated concentrations of L_{AB} and $L^{\dagger}_{AB}$ in the A:B-droplet using the reaction-diffusion simulation. The white broken-line circle indicates the surface of the A:B-droplet. (**f** and **g**) Time courses of the total linker DNA concentration of the A:B-droplet in the numerical simulation via changing the $c_{E_{RH}}$ or $u^0_{R^{\dagger}_{ABi}}$, respectively.

Normalized RNA concentration $\tilde{c}_{AB} = u^0_{R^{\dagger}_{ABi}}/u^0_{T^{\dagger}_{ABi}}$ is defined for numerical simulations. (f) $c_{E_{RH}}$ = 1.25, 2.5, and 5.0 ×10⁻² U/μL; $\tilde{c}_{AB}$ = 1.5. (g) $c_{E_{RH}}$ = 2.5×10⁻² U/μL; $\tilde{c}_{AB}$ = 1.0, 1.5, and 2.0. (**h** and **i**) Time courses of the division ratio r_{div} in the reaction-diffusion simulation with changing the $c_{E_{RH}}$ or $u^0_{R^{\dagger}_{ABi}}$, respectively. (h) $c_{E_{RH}}$ = 1.25, 2.5, and 5.0 ×10⁻² U/μL; $\tilde{c}_{AB}$ = 1.5. (i) $c_{E_{RH}}$ = 2.5×10⁻² U/μL; $\tilde{c}_{AB}$ = 1.0, 1.5, and 2.0.

Experimental investigations of timing-control of DNA droplet division

We performed the experiments shown in Figure 3c for the timing-controlled division of the A:B-droplets. The droplet division reaction started by adding active triggers (T_{ABi}), inhibited triggers ($iT^{\dagger}_{ABi}$), excess inhibitors ($R^{\dagger}_{ABi}$), and RNase H into an A:B-droplet solution (Methods in detail). Figures 4a and 4b show time-lapse images of A:B-droplet division. The required time for the division was elongated with decreasing $c_{E_{RH}}$ or increasing $u^0_{R^{\dagger}_{ABi}}$. Furthermore, we quantified the division ratio r_{div} of the A:B-droplet using image processing (see Supplemental Note S3) (Figures 4c and 4d). r_{div} is 0 if the A- and B-droplets are fully mixed in the A:B-droplets, and 1 if the A:B-droplets are completely divided into A- and B-droplets. The results demonstrated that the increasing

12

rate of r_{div} became slower with decreasing $c_{\mathrm{E_{RH}}}$ or increasing $u^0_{\mathrm{R}^\dagger_{\mathrm{AB}i}}$, which is consistent with the numerical simulation results. Thus, we concluded that the timing-controlled division of DNA droplets was achieved using a time-delay circuit.
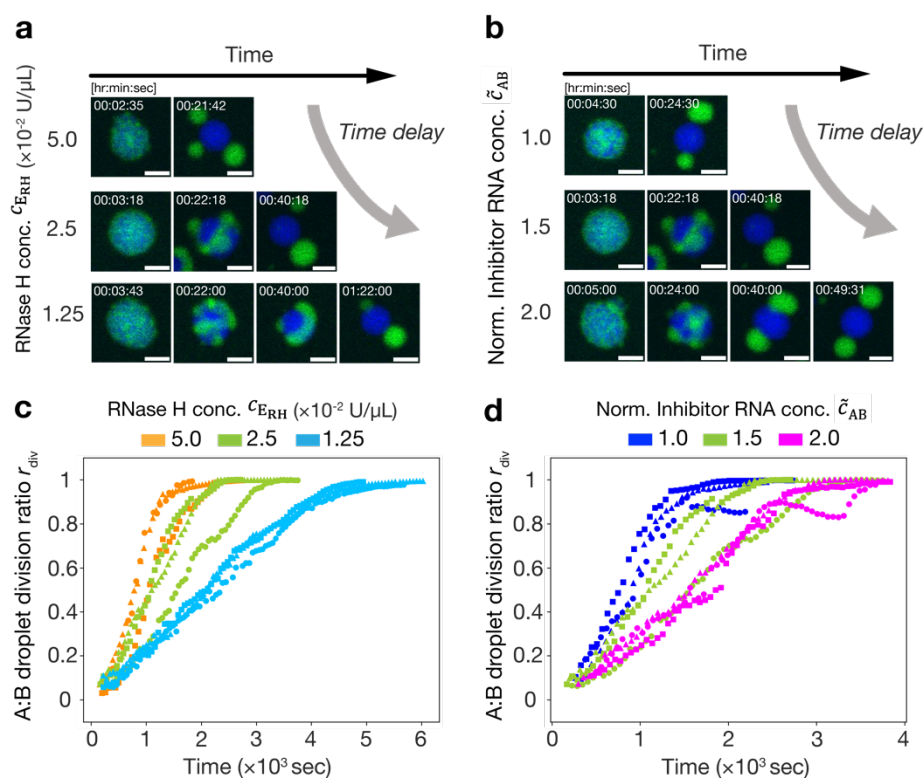

Figure 4. Timing-controlled division of an A:B-droplet coupling with time-delay circuit. (**a** and **b**) Time-lapse images of the division of A:B-droplets with changing the $c_{\mathrm{E_{RH}}}$ or $u^0_{\mathrm{R}^\dagger_{\mathrm{AB}i}}$ (i = 1, 2) (see also Supplemental Movie S1-S5). Scale bars: 10 μm. (a) $c_{\mathrm{E_{RH}}}$ = 1.25, 2.5, and 5.0 ×10⁻² U/μL; $\tilde{c}_{\mathrm{AB}}$ = 1.5. (b) $c_{\mathrm{E_{RH}}}$ = 2.5×10⁻² U/μL; $\tilde{c}_{\mathrm{AB}}$ = 1.0, 1.5, and 2.0. (**c** and **d**) Time courses of the division ratio r_{div} with changing the $c_{\mathrm{E_{RH}}}$ or $u^0_{\mathrm{R}^\dagger_{\mathrm{AB}i}}$. (c) $c_{\mathrm{E_{RH}}}$ = 1.25, 2.5 and 5.0 ×10⁻² U/μL; $\tilde{c}_{\mathrm{AB}}$ = 1.5. (d) $c_{\mathrm{E_{RH}}}$ = 2.5×10⁻² U/μL; $\tilde{c}_{\mathrm{AB}}$ = 1.0, 1.5 and 2.0. All concentrations are at the final concentration of the observed samples.

Pathway control of droplet division

13

Next, we applied the time-delay circuit to control the pathway of DNA droplet division (Figure 5a). We used a ternary-mixed C·A·B-droplet, comprising three types of Y-shaped branched DNA nanostructures (Y_C, Y_A, and Y_B) connected with two types of linkers ($L^\dagger_{AC}$ and $L^\dagger_{AB}$) (Figure 5b). Y_A, Y_B, and $L^\dagger_{AB}$ are the same as those used in the previously described experiment; $L^\dagger_{AC}$ was designed to crosslink Y_C and Y_A. From the viewpoint of the reaction landscape shown in Figure 5a, the C·A·B-droplet has two different pathways (Pathways 1 and 2) for complete division into C-, A-, and B-droplets. Pathway control was achieved by changing the inhibited division triggers (Figure 5c). In Pathway 1, the release of $T^\dagger_{ABi}$ is inhibited; only the C-droplet is divided from the C·A·B-droplet via cleaving $L^\dagger_{AC}$ earlier before the complete division. In Pathway 2, the release of $T^\dagger_{ACi}$ is inhibited; the B-droplet is divided from the C·A·B-droplet via cleaving $L^\dagger_{AB}$ earlier.

Figures 5d and 5e show time-lapse images before and after adding the division triggers. To achieve Pathway 1, we added active triggers $T^\dagger_{ACi}$ (for cleaving $L^\dagger_{AC}$ earlier); inhibited triggers $iT^\dagger_{ABi}$, excess inhibitors $R^\dagger_{ABi}$, and RNase H (for cleaving $L^\dagger_{AB}$ later). Supplemental Movie S6 shows that the order of the division of C- and B-droplets was successfully controlled, as follows. Ternary-mixed C·A·B-droplets (Figure 5d, before addition) divided into C-droplets and binary-mixed A·B-droplets approximately 10 min after the addition (Figure 5d (i)). After another 50 min, the A·B-droplets were divided into A- and B-droplets (Figure 5d (ii)). This indicates that Pathway 1 was selected via the inhibition of $T^\dagger_{ABi}$ due to the presence of $R^\dagger_{ABi}$ (miR-6875-5p and miR-4634). Next, to achieve Pathway 2, we added active triggers $T^\dagger_{ABi}$ (for cleaving $L^\dagger_{AB}$ earlier); inhibited triggers $iT^\dagger_{ACi}$, excess inhibitors $R^\dagger_{ACi}$, and RNase H (for cleaving $L^\dagger_{AC}$ later). For $R^\dagger_{ACi}$, miRNA sequences, miR-1246 and miR-1307-3p, were used (Supplemental Table S3). Supplemental Movie S7 shows that the order of the division of B- and C-droplets was also controlled well. The C·A·B-droplets were first divided into B-droplets and C·A-droplets approximately 30 min after the addition (Figure 5e (i)). After another 20 min, the C·A-droplets were divided into A- and C-droplets (Figure 5e (ii)). This indicates that Pathway 2 was selected because of the presence of $R^\dagger_{ACi}$ (miR-1246 and miR-1307-3p). Thus, the pathway-controlled division was achieved using time-delay circuits.
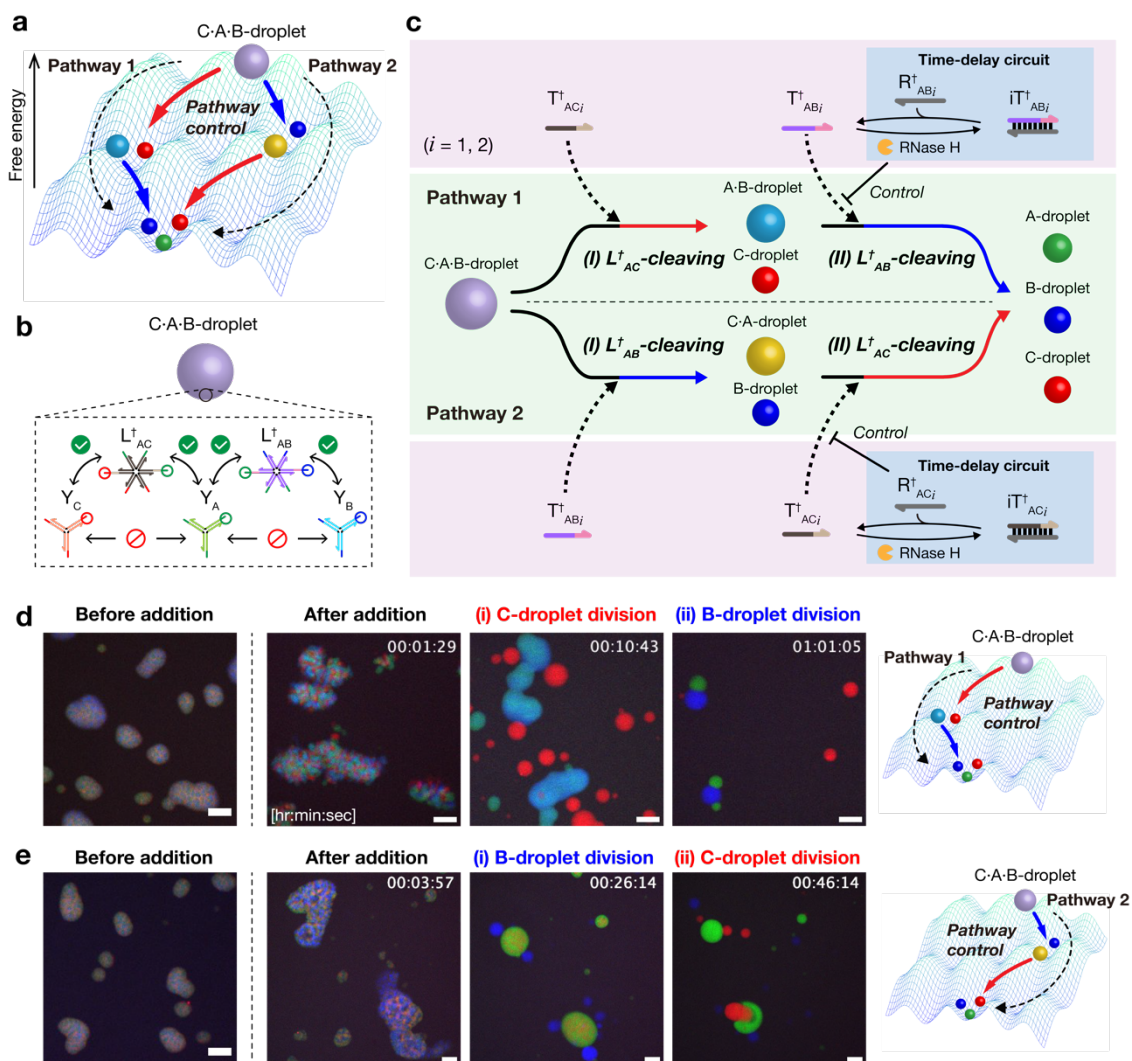
Figure 5. Control of droplet division pathway. (**a**) A reaction landscape of the division of ternary-mixed DNA droplets. The division pathway indicates the order of droplet division. (**b**) Formation of ternary-mixed DNA droplet (C·A·B-droplet) containing three types of Y-shaped DNA nanostructures and two types of DNA linkers. (**c**) Schematic of pathway-controlled division of C·A·B-droplet. The linker-cleavage reaction rates decide the order of droplet division, thereby changing the pathway of droplet division. (**d**) Time-lapse images of C·A·B-droplet division in Pathway 1 before and after adding $T^{\dagger}_{ACi}$, $iT^{\dagger}_{ABi}$, $R^{\dagger}_{ABi}$, and RNase H. The detail of multistep division process is shown in Supplemental Movie S6. $R^{\dagger}_{ABi}$ (*i*=1,2): miR-6875-5p and miR-4634. Scale bars: 20 μm. (**e**) Time-lapse images of C·A·B-droplet division in Pathway 2 before and after adding $T^{\dagger}_{ABi}$, $iT^{\dagger}_{ACi}$, $R^{\dagger}_{ACi}$, and RNase H. The detail of multistep division process is shown in Supplemental Movie S7. $R^{\dagger}_{ACi}$ (*i*=1,2): miR-1246 and miR-1307-3p. Scale bars: 20 μm.

15

Molecular computation: Application of pathway control of droplet division

Finally, we applied the pathway control of droplet division to a molecular computing element "comparator" of RNA concentrations (Figure 6a). Figure 6b shows the reaction scheme of the division pathway of the C·A·B-droplet; the pathway is switched depending on the difference between two normalized initial concentrations of inhibitor RNAs:

$\tilde{c}_{AB} = u^0_{R^\dagger_{ABi}}/u^0_{T^\dagger_{ABi}}$ and $\tilde{c}_{AC} = u^0_{R^\dagger_{ACi}}/u^0_{T^\dagger_{ACi}}$ (i=1,2), which are for the cleavage delay of $L^\dagger_{AB}$ and $L^\dagger_{AC}$, respectively. The comparator accepts miRNA sequences (Figure 6a) as inputs; i.e., the input miRNAs work as the inhibitor RNAs, $R^\dagger_{ABi}$ and $R^\dagger_{ACi}$ (Figure 6b). Theoretically, if $\tilde{c}_{AB} > \tilde{c}_{AC}$, Pathway 1 is selected; the $L^\dagger_{AB}$ cleavage delays longer than the $L^\dagger_{AC}$ because more $R^\dagger_{ABi}$ causes a longer time delay (Figure 6b). Contrarily, if $\tilde{c}_{AB} < \tilde{c}_{AC}$, Pathway 2 is selected; the $L^\dagger_{AC}$ cleavage delays longer. Thus, the observed pathway indicates the result of the comparison between $\tilde{c}_{AB}$ and $\tilde{c}_{AC}$ (Figure 6a).

Comparator experiments were performed using several RNA concentrations. Here, we define $\Delta\tilde{c} = \tilde{c}_{AB} - \tilde{c}_{AC}$ and $\tilde{c}_t = \tilde{c}_{AB} + \tilde{c}_{AC}$. We investigated five types of conditions of the initial RNA concentrations shown in Figure 6c: $(\Delta\tilde{c}; \tilde{c}_{AB}, \tilde{c}_{AC}; \tilde{c}_t) =$ $(1.25; 1.25, 0; 1.25)$ (i), $(0.5; 1.25, 0.75; 2.0)$ (ii), $(-0.5; 0.75, 1.25; 2.0)$ (iii), $(-1.0; 0.25, 1.25; 1.5)$ (iv), and $(-1.25; 0, 1.25; 1.25)$ (v). Under conditions (i)–(iii), the C-droplet divided first, whereas under conditions (iv) and (v), the B-droplet divided first (Supplemental Figure S3). Figure 6c shows the time courses of the division ratios of B- (r_{div_B}) and C- (r_{div_C}) droplets quantified using the image processing method shown in Supplementary Note S3. These results showed that with higher $\Delta\tilde{c}$, C-droplet division was faster. Note that an increase in $\tilde{c}_t$ caused a delay in the overall reaction, probably because more RNA molecules induced competition in the degradation of RNA by RNase H in the condition of the same RNase H concentration.

For quantitative estimation, we calculated the time difference $\Delta\tau$ between the division timings of B- and C-droplets (Figures 6d): $\Delta\tau = \tau_{div\_B} - \tau_{div\_C}$, where τ_{div_B} and τ_{div_C} are defined as the times when r_{div_B} and r_{div_C} were both approximately 0.5, respectively. As shown in Figure 6d, $\Delta\tau > 0$ was observed when the RNA concentration difference $\Delta\tilde{c} = 1.25$ (i), 0.5 (ii), and -0.5 (iii), indicating that the division occurred through Pathway 1. Alternatively, $\Delta\tau < 0$ was observed when $\Delta\tilde{c} = -1.0$ (iv) and

16

-1.25 (v), indicating that Pathway 2 was selected. These results demonstrated that the division pathway changed depending on the RNA concentration differences, confirming that the concentration comparator for the miRNA sequences worked as expected.

Ideally, the sign of $\Delta\tau$ is expected to switch when $\Delta\tilde{c} = 0$. However, the results imply that the sign switches between $\Delta\tilde{c} = -0.5$ and -1.0 (i.e., $\Delta\tilde{c} \neq 0$). Here, we define an offset concentration of this molecular comparator, σ, at which the sign of $\Delta\tau$ switches, where the output of the comparator switches. Regular electrical comparators generally have a non-zero offset voltage because of non-ideal circuit properties; similarly, our molecular comparator has a non-zero offset ($\sigma \neq 0$). $\sigma \neq 0$ would be observed probably because B-droplet division took longer than that of the C-droplet for some reasons; for example, the DNA sequence difference induced the slower cleavage of $L^{\dagger}_{AB}$ than $L^{\dagger}_{AC}$, or more linker cleavage is required for B-droplet division than C-droplet division. In future studies, σ may be tuned by sequence designing of DNAs.

To estimate the hypothesis for the mechanism of the non-zero offset, we performed numerical simulations using a reaction-diffusion model that considered differences in the cleavage rate of linker DNAs (see Supplemental Note S2). First, we changed the hybridization and the strand displacement rates for $L^{\dagger}_{AB}$ cleavage. Next, we varied the threshold parameters K_{AB} and K_{AC} for r_{div_B} and r_{div_C} (Eqs. S.90 and S.91 in Supplemental Note S2); the larger the threshold parameters, the faster the division.

We set the hybridization rate and the strand displacement rate between $T^{\dagger}_{ABi}$ and $L^{\dagger}_{AB}$ to be 10 times lower than that between $T^{\dagger}_{ACi}$ and $L^{\dagger}_{AC}$. K_{AB} and K_{AC} are set to asymmetric values of 0.1, and 0.9, respectively. Figure 6e shows the time courses of r_{div_B} and r_{div_C} in the simulation results. As $\Delta\tilde{c}$ increased, the C-droplets tended to divide earlier. Additionally, as shown in Figure 6f, the offset concentration σ was approximately -0.5, indicating that the trend is consistent with the experimental result. These results suggest that the differences in the cleavage rate between $L^{\dagger}_{AB}$ and $L^{\dagger}_{AC}$ and the required amount of linker cleavage for B-droplet and C-droplet divisions resulted in $\sigma \neq 0$. Furthermore, numerical simulations were performed using different parameter values (Supplemental Figures S4-S6), producing different offset concentrations. These results suggest that changing DNA sequences could potentially control the offset concentration σ. Note that, when more $\tilde{c}_t$, the simulation results reproduce the delay in the overall reaction as observed in experiments due to the competition in the RNase H reaction.
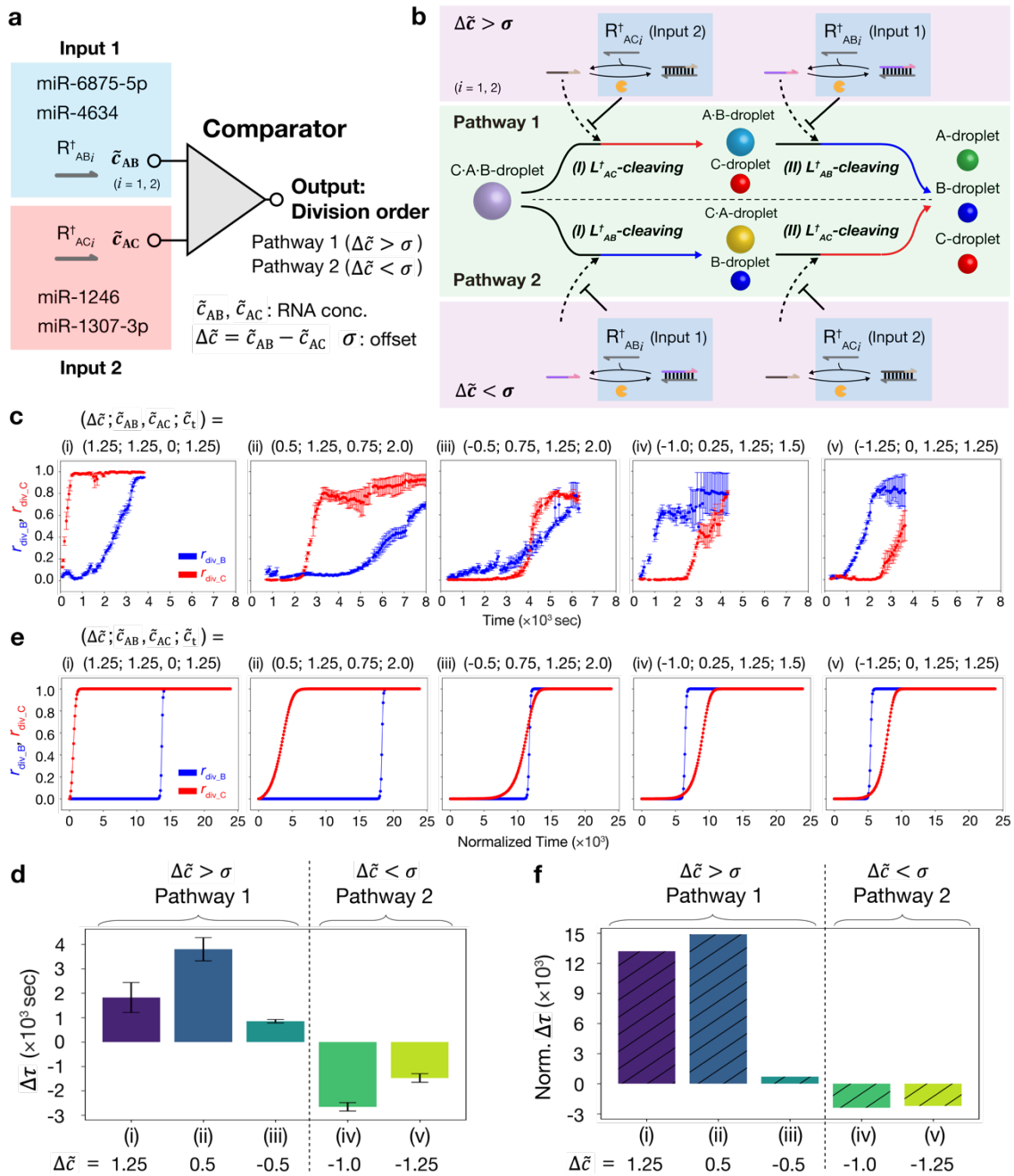
17

Figure 6. Application of pathway control to a molecular comparator for miRNA concentrations. (**a**) Concept of a molecular comparator of miRNA concentrations. miRNAs miR-6875-5p and miR-4634 were used for input 1 for the comparator; miR-1246 and miR-1307-3p were used for the input 2. In this experiment, $u^0_{R^\dagger_{AB1}} =$ [miR-6875-5p], $u^0_{R^\dagger_{AB2}} =$ [miR-4634], and $u^0_{R^\dagger_{AB1}} = u^0_{R^\dagger_{AB2}}$; $u^0_{R^\dagger_{AC1}} =$ [miR-1246],

18

$u^0_{R^\dagger_{AC2}}$ = [miR-1307-3p], and $u^0_{R^\dagger_{AC1}} = u^0_{R^\dagger_{AC2}}$. (**b**) Schematic of pathway-controlled division of the C·A·B-droplet using two types of time-delay circuits. The pathway of droplet division is changed by the order of linker cleavages depending on the difference between two normalized inhibitor RNA concentrations $\tilde{c}_{AB} = u^0_{R^\dagger_{ABi}}/u^0_{T^\dagger_{ABi}}$ and

$\tilde{c}_{AC} = u^0_{R^\dagger_{ACi}}/u^0_{T^\dagger_{ACi}}$ (*i*=1, 2). (**c**) Time courses of $r_{\text{div\_B}}$ (blue) and $r_{\text{div\_C}}$ (red) at varying the inhibitor RNA concentrations in the experiment. Total initial RNA concentration $\tilde{c}_t$ is defined as $\tilde{c}_t = \tilde{c}_{AB} + \tilde{c}_{AC}$. The $\Delta\tilde{c}$ $(= \tilde{c}_{AB} - \tilde{c}_{AC})$ was varied at (i) 1.25, (ii) 0.5, (iii) −0.5, (iv) −1.0, and (v) −1.25. RNase H concentration was fixed at 0.25 U/μL in all experiments. (**d**) Time difference $\Delta\tau$ at each of five RNA conditions (i)-(v) in the experiment. (**e**) Time courses of $r_{\text{div\_B}}$ (blue) and $r_{\text{div\_C}}$ (red) at varying inhibitor RNA concentrations in the reaction-diffusion simulation. The $\Delta\tilde{c}$ was varied at (i) 1.25, (ii) 0.5, (iii) − 0.5, (iv) − 1.0, and (v) − 1.25. The hybridization rate and the strand displacement rate between $T^\dagger_{ABi}$ and $L^\dagger_{AB}$ were set 10 times lower than those between $T^\dagger_{ACi}$ and $L^\dagger_{AC}$, respectively. Threshold parameters K_{AB} and K_{AC} were set as 0.1 and 0.9, respectively. (**f**) Time difference $\Delta\tau$ at each of five RNA conditions (i)-(v) in the reaction-diffusion simulation.

Conclusion

We demonstrated the timing-controlled division dynamics of DNA droplets using a time-delay circuit. We developed the reaction-diffusion model and numerically investigated the strategy to control the division timing by controlling the cleavage rate of $L^\dagger_{AB}$. Using this strategy, we experimentally demonstrated timing control of the division of an A:B-droplet by tuning the time-delay circuit parameters. We realized the pathway control of the C·A·B-droplet division by changing the order of two types of linker DNA cleavage based on the time-delay circuit. Finally, we employed the pathway control of the C·A·B-droplet division for molecular computation and achieved a comparator of miRNA concentrations, which may be applied to a diagnosis based on the concentration difference of expressed miRNAs.

The RNA concentration comparator had non-zero offset ($\sigma \neq 0$) (Figure 6d), and the simulation results suggested that σ changed depending on hybridization rates or strand

displacement rates of linker DNAs (Figure 6f and Supplemental Figures S4-S6). Because the hybridization and strand displacement rates of DNAs depend on their sequence and length[55], these results suggest that the non-zero offset was probably due to the sequences of the linker DNA nanostructure. Previously, Saleh et al.[58] and Sato et al.[57] have shown that differences in the sequences of DNA nanostructures changed the kinetic and thermodynamic properties of DNA droplets. To further control the DNA droplet dynamics, the influence of DNA sequences on the kinetic properties of DNA nanostructures must be clarified.

The present study demonstrated that non-equilibrium chemical reactions could control DNA droplet dynamics such as droplet division. In future, the control of chemical reactions via the physical dynamics of DNA droplets should be explored. Such bidirectional control over more complex dynamics can help build artificial cells with more living cell-like functions, such as biochemical reactions controlled by the condensates of transcriptional factors and cell/organelle behaviors controlled by transcripts[6,59]. Moreover, enzymatic reactions regulated by synthetic protein-based coacervates[60] can be combined with our DNA-based droplet system. We believe that this technology provides a new strategy to create artificial cells and molecular robots with more sophisticated functions, such as timing-controlled self-replication, drug delivery, and diagnosis, with more accuracy and quantitative specifications.

Materials and Methods

Sequence design and oligo-nucleotides preparation

DNA and RNA sequences were designed using the Nucleic Acid Package (NUPACK)[61]. All oligonucleotide sequences listed in Tables S1-S3 were purchased from Eurofins Genomics (Tokyo, Japan). The fluorescently labeled DNA was purified using high-performance liquid chromatography (HPLC), while the others were purified using an oligonucleotide purification cartridge (OPC). The purchased oligonucleotide powders were diluted to 100 or 200 μM with ultra-pure water (Direct-Q UV, Millipore, ZRQSVP030) and stored at -20°C.

Preparation of mixed DNA droplets

We prepared three DNA droplets (A·B-droplet, A:B-droplet, C·A·B-droplet). In Figures 2c and 2g, a sample solution for the A·B-droplet contained 5 μM Y_A, 5 μM Y_B, and 1.65 μM L_{AB} in a reaction buffer (20 mM Tris-HCl [pH 8.0], 350 mM NaCl) was heated at 85°C for 5 min and then cooled down from 85°C to 25°C at a rate of −1°C/min to anneal the contained DNAs using a thermal cycler (Mastercycler® nexus X2, Eppendorf, Germany). In Figures 4a and 4b, a sample solution for the A:B-droplet contained 5 μM Y_A, 5 μM Y_B, 1.485 μM L_{AB}, and 0.165 μM $L^{\dagger}_{AB}$ in the reaction buffer was heated and cooled down in the same manner. In Figures 5d and 5e, a sample solution for the C·A·B-droplet contained 1.0 μM Y_A, 1.0 μM Y_B, 1.0 μM Y_C, 2.0 μM $L^{\dagger}_{AB}$, and 2 μM $L^{\dagger}_{AC}$ in the reaction buffer was heated and cooled down in the same manner. After annealing, the sample of the A·B-droplet and A:B-droplet were diluted twofold with the reaction buffer. The C·A·B-droplet was not diluted. The concentrations of each strand in the mixed DNA droplet after dilution and addition of the division trigger mixture are shown in Supplemental Tables S4-S6. Tris-HCl (pH 8.0) (cat. #15568025) were purchased from Invitrogen (Carlsbad, CA), and NaCl (cat. #191-01665) was purchased from Wako (Japan), respectively.

Microscopy Observation

To observe the autonomous division of the A·B-droplet samples and the timing-controlled division of the A:B-droplet samples, we used a confocal laser scanning microscopy (CLSM) (FV-1000, Olympus, Tokyo, Japan) and a stage heater (10021-PE120 system, Linkam, Fukuoka, Japan). To observe the pathway-controlled division of the C·A·B-droplet, we used fluorescent microscopy (IX-71, Olympus, Tokyo, Japan)

21

equipped with a spinning-disk confocal system (CSU-X1, Yokogawa, Tokyo, Japan), an EM CCD camera (iXon X3, Andor), and the stage heater. Samples containing 6-FAM, Alexa 405, and Cy3 were visualized at excitation wavelengths of 473, 405, and 561 nm, respectively. Observation chambers were prepared for CLSM observation. Glass slides (dimensions: 30 × 40 mm, thickness: 0.17 mm, Matsunami, Kishiwada, Japan) were soaked in 5% bovine serum albumin (BSA) (cat. #019-15123, Wako, Japan) solution with 20 mM Tris-HCl (pH 8.0) for 30 min. After BSA coating, the glasses were washed with ultrapure water and dried. The 1-mm-thickness silicon sheet (cat. #107-0040202, Kokugo, Japan) with 5 mm-diameter holes was placed on the BSA-coated glass.

Timing-controlled division experiments of binary-mixed DNA droplets by adding a division trigger solution

In Figures 4a and 4b, 3 µL of the A:B-droplet sample solution was placed in the 5 mm hole of the observation chamber. The sample solutions were covered with mineral oil to prevent evaporation. The chamber was incubated on a stage heater at 60°C for 30 min to increase the fluidity of the DNA droplets. After incubation, we added a division trigger mixture to the sample solution in the chamber and observed it at 60°C. Depending on the experiment, different division trigger contents and concentrations were used in the division trigger mixtures. When the final concentration of RNase H ($c_{E_{RH}}$) was fixed at

2.5×10^{-2} U/µL, the normalized RNA concentration ($\tilde{c}_{AB} = u^0_{R^\dagger_{AB1}}/u^0_{T^\dagger_{AB1}} = u^0_{R^\dagger_{AB2}}/$

$u^0_{T^\dagger_{AB2}}$) at the final concentration was varied as 1, 1.5, and 2. When the $\tilde{c}_{AB}$ at the final concentration was fixed at 1.5, the $c_{E_{RH}}$ was varied as 1.25×10^{-2}, 2.5×10^{-2}, and 5.0×10^{-2} U/µL. To calculate the division rate, r_{div}, we binarized the fluorescent images and analyzed them using Fiji[62]. The experimental details are described in Supplemental Methods S2.

Pathway-controlled division experiments of ternary-mixed DNA droplets by adding a division trigger solution

C·A·B-droplet sample solution (2.4 µL) was placed in the 5 mm hole of the observation chamber. The sample solutions were covered with mineral oil to prevent evaporation. The chamber was incubated on a stage heater at 60°C for 30 min and 63°C for 15 min to increase the fluidity of the DNA droplets. After incubation, we added 3.6 µL of a division trigger mixture to the sample solution in the chamber and observed it at 63°C. Depending on the experiment, different division trigger contents and concentrations were used in the

division trigger mixtures. The experimental details are described in Supplemental Methods S3.

23

Acknowledgment

References

(1) Alberts, B. *Molecular Biology of the Cell*; Garland Science, 2017.

(2) Shin, Y.; Brangwynne, C. P. Liquid Phase Condensation in Cell Physiology and Disease. *Science* **2017**, *357* (6357). https://doi.org/10.1126/science.aaf4382.

(3) Banani, S. F.; Lee, H. O.; Hyman, A. A.; Rosen, M. K. Biomolecular Condensates: Organizers of Cellular Biochemistry. *Nat. Rev. Mol. Cell Biol.* **2017**, *18* (5), 285–298.

(4) Falahati, H.; Pelham-Webb, B.; Blythe, S.; Wieschaus, E. Nucleation by RRNA Dictates the Precision of Nucleolus Assembly. *Curr. Biol.* **2016**, *26* (3), 277–285.

(5) Brangwynne, C. P.; Mitchison, T. J.; Hyman, A. A. Active Liquid-like Behavior of Nucleoli Determines Their Size and Shape in Xenopus Laevis Oocytes. *Proc. Natl. Acad. Sci. U. S. A.* **2011**, *108* (11), 4334–4339.

(6) Sabari, B. R.; Dall'Agnese, A.; Boija, A.; Klein, I. A.; Coffey, E. L.; Shrinivas, K.; Abraham, B. J.; Hannett, N. M.; Zamudio, A. V.; Manteiga, J. C.; Li, C. H.; Guo, Y. E.; Day, D. S.; Schuijers, J.; Vasile, E.; Malik, S.; Hnisz, D.; Lee, T. I.; Cisse, I. I.; Roeder, R. G.; Sharp, P. A.; Chakraborty, A. K.; Young, R. A. Coactivator Condensation at Super-Enhancers Links Phase Separation and Gene Control. *Science* **2018**, *361* (6400). https://doi.org/10.1126/science.aar3958.

(7) Martin, N. Dynamic Synthetic Cells Based on Liquid-Liquid Phase Separation. *Chembiochem* **2019**, *20* (20), 2553–2568.

(8) Lin, Z.; Beneyton, T.; Baret, J.-C.; Martin, N. Coacervate Droplets for Synthetic Cells. *Small Methods* **2023**, e2300496.

(9) Zhang, S.; Contini, C.; Hindley, J. W.; Bolognesi, G.; Elani, Y.; Ces, O. Engineering Motile Aqueous Phase-Separated Droplets via Liposome Stabilisation. *Nat. Commun.* **2021**, *12* (1), 1673.

(10) Schuster, B. S.; Reed, E. H.; Parthasarathy, R.; Jahnke, C. N.; Caldwell, R. M.; Bermudez, J. G.; Ramage, H.; Good, M. C.; Hammer, D. A. Controllable Protein

Phase Separation and Modular Recruitment to Form Responsive Membraneless Organelles. *Nat. Commun.* **2018**, *9* (1), 2985.

(11) Mu, W.; Ji, Z.; Zhou, M.; Wu, J.; Lin, Y.; Qiao, Y. Membrane-Confined Liquid-Liquid Phase Separation toward Artificial Organelles. *Sci Adv* **2021**, *7* (22). https://doi.org/10.1126/sciadv.abf9000.

(12) Liu, S.; Zhang, Y.; Li, M.; Xiong, L.; Zhang, Z.; Yang, X.; He, X.; Wang, K.; Liu, J.; Mann, S. Enzyme-Mediated Nitric Oxide Production in Vasoactive Erythrocyte Membrane-Enclosed Coacervate Protocells. *Nat. Chem.* **2020**, *12* (12), 1165–1173.

(13) Tsumoto, K.; Arai, M.; Nakatani, N.; Watanabe, S. N.; Yoshikawa, K. Does DNA Exert an Active Role in Generating Cell-Sized Spheres in an Aqueous Solution with a Crowding Binary Polymer? *Life* **2015**, *5* (1), 459–466.

(14) Lin, Y.; Jing, H.; Liu, Z.; Chen, J.; Liang, D. Dynamic Behavior of Complex Coacervates with Internal Lipid Vesicles under Nonequilibrium Conditions. *Langmuir* **2020**, *36* (7), 1709−1717.

(15) Matsuo, M.; Kurihara, K. Proliferating Coacervate Droplets as the Missing Link between Chemistry and Biology in the Origins of Life. *Nat. Commun.* **2021**, *12* (1), 5487.

(16) Saleh, O. A.; Wilken, S.; Squires, T. M.; Liedl, T. Vacuole Dynamics and Popping-Based Motility in Liquid Droplets of DNA. *Nat. Commun.* **2023**, *14* (1), 3574.

(17) Sato, Y.; Sakamoto, T.; Takinoue, M. Sequence-Based Engineering of Dynamic Functions of Micrometer-Sized DNA Droplets. *Sci Adv* **2020**, *6* (23), eaba3471.

(18) Donau, C.; Späth, F.; Sosson, M.; Kriebisch, B. A. K.; Schnitter, F.; Tena-Solsona, M.; Kang, H.-S.; Salibi, E.; Sattler, M.; Mutschler, H.; Boekhoven, J. Active Coacervate Droplets as a Model for Membraneless Organelles and Protocells. *Nat. Commun.* **2020**, *11* (1), 5167.

(19) Späth, F.; Donau, C.; Bergmann, A. M.; Kränzlein, M.; Synatschke, C. V.; Rieger, B.; Boekhoven, J. Molecular Design of Chemically Fueled Peptide-Polyelectrolyte Coacervate-Based Assemblies. *J. Am. Chem. Soc.* **2021**, *143* (12), 4782–4789.

(20) Bergmann, A. M.; Bauermann, J.; Bartolucci, G.; Donau, C.; Stasi, M.; Holtmannspötter, A.-L.; Jülicher, F.; Weber, C. A.; Boekhoven, J. Liquid Spherical Shells Are a Non-Equilibrium Steady State of Active Droplets. *Nat. Commun.* **2023**, *14* (1), 6552.

(21) Aumiller, W. M., Jr; Keating, C. D. Phosphorylation-Mediated RNA/Peptide Complex Coacervation as a Model for Intracellular Liquid Organelles. *Nat. Chem.* **2016**, *8* (2), 129–137.

25

(22) Nakashima, K. K.; Baaij, J. F.; Spruijt, E. Reversible Generation of Coacervate Droplets in an Enzymatic Network. *Soft Matter* **2018**, *14* (3), 361–367.

(23) Spoelstra, W. K.; van der Sluis, E. O.; Dogterom, M.; Reese, L. Nonspherical Coacervate Shapes in an Enzyme-Driven Active System. *Langmuir* **2020**, *36* (8), 1956–1964.

(24) Hong, F.; Zhang, F.; Liu, Y.; Yan, H. DNA Origami: Scaffolds for Creating Higher Order Structures. *Chem. Rev.* **2017**, *117* (20), 12584–12640.

(25) Dong, Y.; Yao, C.; Zhu, Y.; Yang, L.; Luo, D.; Yang, D. DNA Functional Materials Assembled from Branched DNA: Design, Synthesis, and Applications. *Chem. Rev.* **2020**, *120* (17), 9420–9481.

(26) Kieffer, C.; Genot, A. J.; Rondelez, Y.; Gines, G. Molecular Computation for Molecular Classification. *Adv Biol (Weinh)* **2023**, e2200203.

(27) Kim, J.; Winfree, E. Synthetic *in Vitro* Transcriptional Oscillators. *Mol. Syst. Biol.* **2011**, *7*, 465.

(28) Montagne, K.; Plasson, R.; Sakai, Y.; Fujii, T.; Rondelez, Y. Programming an in Vitro DNA Oscillator Using a Molecular Networking Strategy. *Mol. Syst. Biol.* **2011**, *7*, 466.

(29) Srinivas, N.; Parkin, J.; Seelig, G.; Winfree, E.; Soloveichik, D. Enzyme-Free Nucleic Acid Dynamical Systems. *Science* **2017**, *358* (6369). https://doi.org/10.1126/science.aal2052.

(30) Lapteva, A. P.; Sarraf, N.; Qian, L. DNA Strand-Displacement Temporal Logic Circuits. *J. Am. Chem. Soc.* **2022**, *144* (27), 12443–12449.

(31) Bucci, J.; Irmisch, P.; Del Grosso, E.; Seidel, R.; Ricci, F. Orthogonal Enzyme-Driven Timers for DNA Strand Displacement Reactions. *J. Am. Chem. Soc.* **2022**. https://doi.org/10.1021/jacs.2c06599.

(32) Bucci, J.; Irmisch, P.; Del Grosso, E.; Seidel, R.; Ricci, F. Timed Pulses in DNA Strand Displacement Reactions. *J. Am. Chem. Soc.* **2023**, *145* (38), 20968–20974.

(33) Shin, J.-S.; Pierce, N. A. A Synthetic DNA Walker for Molecular Transport. *J. Am. Chem. Soc.* **2004**, *126* (35), 10834–10835.

(34) Andersen, E. S.; Dong, M.; Nielsen, M. M.; Jahn, K.; Subramani, R.; Mamdouh, W.; Golas, M. M.; Sander, B.; Stark, H.; Oliveira, C. L. P.; Pedersen, J. S.; Birkedal, V.; Besenbacher, F.; Gothelf, K. V.; Kjems, J. Self-Assembly of a Nanoscale DNA Box with a Controllable Lid. *Nature* **2009**, *459* (7243), 73–76.

(35) Pumm, A.-K.; Engelen, W.; Kopperger, E.; Isensee, J.; Vogt, M.; Kozina, V.; Kube, M.; Honemann, M. N.; Bertosin, E.; Langecker, M.; Golestanian, R.; Simmel, F. C.;

Dietz, H. A DNA Origami Rotary Ratchet Motor. *Nature* **2022**, *607* (7919), 492–498.

(36) Udono, H.; Gong, J.; Sato, Y.; Takinoue, M. DNA Droplets: Intelligent, Dynamic Fluid. *Adv Biol (Weinh)* **2022**, e2200180.

(37) Takinoue, M. DNA Droplets for Intelligent and Dynamical Artificial Cells: From the Viewpoint of Computation and Non-Equilibrium Systems. *Interface Focus* **2023**, *13* (5), 20230021.

(38) Jeon, B.-J.; Nguyen, D. T.; Abraham, G. R.; Conrad, N.; Fygenson, D. K.; Saleh, O. A. Salt-Dependent Properties of a Coacervate-like, Self-Assembled DNA Liquid. *Soft Matter* **2018**, *14* (34), 7009–7015.

(39) Jeon, B.-J.; Nguyen, D. T.; Saleh, O. A. Sequence-Controlled Adhesion and Microemulsification in a Two-Phase System of DNA Liquid Droplets. *J. Phys. Chem. B* **2020**, *124* (40), 8888–8895.

(40) Sato, Y.; Takinoue, M. Capsule-like DNA Hydrogels with Patterns Formed by Lateral Phase Separation of DNA Nanostructures. *JACS Au* **2022**, *2* (1), 159–168.

(41) Tran, M. P.; Chatterjee, R.; Dreher, Y.; Fichtler, J.; Jahnke, K.; Hilbert, L.; Zaburdaev, V.; Göpfrich, K. A DNA Segregation Module for Synthetic Cells. *Small* **2022**, e2202711.

(42) Agarwal, S.; Osmanovic, D.; Klocke, M. A.; Franco, E. The Growth Rate of DNA Condensate Droplets Increases with the Size of Participating Subunits. *ACS Nano* **2022**. https://doi.org/10.1021/acsnano.2c00084.

(43) Lee, T.; Do, S.; Lee, J. G.; Kim, D.-N.; Shin, Y. The Flexibility-Based Modulation of DNA Nanostar Phase Separation. *Nanoscale* **2021**, *13* (41), 17638–17647.

(44) Zhao, Q.-H.; Cao, F.-H.; Luo, Z.-H.; Huck, W. T. S.; Deng, N.-N. Photoswitchable Molecular Communication between Programmable DNA-Based Artificial Membraneless Organelles. *Angew. Chem. Int. Ed Engl.* **2022**, *61* (14), e202117500.

(45) Deng, J.; Walther, A. Programmable ATP-Fueled DNA Coacervates by Transient Liquid-Liquid Phase Separation. *Chem* **2020**, *6* (12), 3329–3343.

(46) Saleh, O. A.; Jeon, B.-J.; Liedl, T. Enzymatic Degradation of Liquid Droplets of DNA Is Modulated near the Phase Boundary. *Proc. Natl. Acad. Sci. U. S. A.* **2020**, *117* (28), 16160–16166.

(47) Gong, J.; Tsumura, N.; Sato, Y.; Takinoue, M. Computational DNA Droplets Recognizing MiRNA Sequence Inputs Based on Liquid–Liquid Phase Separation. *Adv. Funct. Mater.* **2022**, 2202322.

(48) Leathers, A.; Walczak, M.; Brady, R. A.; Al Samad, A.; Kotar, J.; Booth, M. J.; Cicuta, P.; Di Michele, L. Reaction–Diffusion Patterning of DNA-Based Artificial Cells. *J. Am. Chem. Soc.* **2022**. https://doi.org/10.1021/jacs.2c06140.

(49) Kim, J.; White, K. S.; Winfree, E. Construction of an *in Vitro* Bistable Circuit from Synthetic Transcriptional Switches. *Mol. Syst. Biol.* **2006**, *2* (1), 68.

(50) Takinoue, M.; Kiga, D.; Shohda, K.-I.; Suyama, A. Experiments and Simulation Models of a Basic Computation Element of an Autonomous Molecular Computing System. *Phys. Rev. E* **2008**, *78* (4), 041921.

(51) Wang, Y.; Hu, N.; Liu, C.; Nie, C.; He, M.; Zhang, J.; Yu, Q.; Zhao, C.; Chen, T.; Chu, X. An RNase H-Powered DNA Walking Machine for Sensitive Detection of RNase H and the Screening of Related Inhibitors. *Nanoscale* **2020**, *12* (3), 1673–1679.

(52) Legewie, S.; Dienst, D.; Wilde, A.; Herzel, H.; Axmann, I. M. Small RNAs Establish Delays and Temporal Thresholds in Gene Expression. *Biophys. J.* **2008**, *95* (7), 3232–3238.

(53) Shimomura, A.; Shiino, S.; Kawauchi, J.; Takizawa, S.; Sakamoto, H.; Matsuzaki, J.; Ono, M.; Takeshita, F.; Niida, S.; Shimizu, C.; Fujiwara, Y.; Kinoshita, T.; Tamura, K.; Ochiya, T. Novel Combination of Serum MicroRNA for Detecting Breast Cancer in the Early Stage. *Cancer Sci.* **2016**, *107* (3), 326–334.

(54) Hirano, N.; Haruki, M.; Morikawa, M.; Kanaya, S. Enhancement of the Enzymatic Activity of Ribonuclease HI from Thermus Thermophilus HB8 with a Suppressor Mutation Method. *Biochemistry* **2000**, *39* (43), 13285–13294.

(55) Zhang, D. Y.; Winfree, E. Control of DNA Strand Displacement Kinetics Using Toehold Exchange. *J. Am. Chem. Soc.* **2009**, *131* (47), 17303–17314.

(56) Lukacs, G. L.; Haggie, P.; Seksek, O.; Lechardeur, D.; Freedman, N.; Verkman, A. S. Size-Dependent DNA Mobility in Cytoplasm and Nucleus. *J. Biol. Chem.* **2000**, *275* (3), 1625–1629.

(57) Sato, Y.; Takinoue, M. Sequence-Dependent Fusion Dynamics and Physical Properties of DNA Droplets. *Nanoscale Adv.* **2023**, *5* (7), 1919–1925.

(58) Nguyen, D. T.; Saleh, O. A. Tuning Phase and Aging of DNA Hydrogels through Molecular Design. *Soft Matter* **2017**, *13* (32), 5421–5427.

(59) Feric, M.; Vaidya, N.; Harmon, T. S.; Mitrea, D. M.; Zhu, L.; Richardson, T. M.; Kriwacki, R. W.; Pappu, R. V.; Brangwynne, C. P. Coexisting Liquid Phases Underlie Nucleolar Subcompartments. *Cell* **2016**, *165* (7), 1686–1697.

(60) Ura, T.; Tomita, S.; Shiraki, K. Dynamic Behavior of Liquid Droplets with Enzyme Compartmentalization Triggered by Sequential Glycolytic Enzyme Reactions. *Chem. Commun.* **2021**, *57* (93), 12544–12547.

(61) Zadeh, J. N.; Steenberg, C. D.; Bois, J. S.; Wolfe, B. R.; Pierce, M. B.; Khan, A. R.; Dirks, R. M.; Pierce, N. A. NUPACK: Analysis and Design of Nucleic Acid Systems. *J. Comput. Chem.* **2011**, *32* (1), 170–173.

(62) Schindelin, J.; Arganda-Carreras, I.; Frise, E.; Kaynig, V.; Longair, M.; Pietzsch, T.; Preibisch, S.; Rueden, C.; Saalfeld, S.; Schmid, B.; Tinevez, J.-Y.; White, D. J.; Hartenstein, V.; Eliceiri, K.; Tomancak, P.; Cardona, A. Fiji: An Open-Source Platform for Biological-Image Analysis. *Nat. Methods* **2012**, *9* (7), 676–682.